Solution-Processed Metal Doping of Sub-3 nm SnO_2 Quantum Wires for Enhanced H_2S Sensing at Low Temperature

Received 00th January 20xx,Received 00th January 20xx, Accepted 00th January 20xx

DOI: 10.1039/x0xx00000x

Jia Yan,[a] Xuyun Guo,[b] Ye Zhu,[b,c] Zhilong Song*,[d] and Lawrence Yoon Suk Lee*,[a,c]

Doping a foreign atom to metal oxides enables the modulations of the electronic and chemical properties of active sites. SnO_2 quantum wires (QWs) possessing large surface area with highly exposed active sites have been demonstrated as promising sensing materials in gas sensors but they still suffer from the unsatisfactory selectivity and limit of detections (LODs). Herein, we realize the electronic interaction of transition metal atoms (Cr, Mo, and W) and sub-3 nm ultrathin SnO_2 QWs using a general one-step solution process at low temperature (180 °C). Density functional theory calculations reveal that such tailored electronic structures reduce energy barriers for adsorption of gas molecules and transportation of electrons, which facilitates oxygen adsorption and activation, and thus accelerates surface reaction kinetics with H_2S molecules. Our results indicate that the transition metal doping induces more oxygen vacancies (V_O) that lead to boosted H_2S chemical-sensing performances. A representative W-doped SnO_2 QWs (W-SnO_2) achieve enhanced low-temperature H_2S-sensing properties with a record LOD of down to 0.48 ppb, which surpasses most of the reported metal oxide-based gas sensors.

Introduction

Chemiresistive gas sensors play important roles in monitoring daily air quality, industrial processes, and health status, as well as in smart home/building/urban applications.[1-3] Tin oxide (SnO_2)-based sensors are one of the most commonly used gas sensors owing to their excellent physicochemical properties, easy operation, and long service life.[4, 5] However, due to the limited number of active sites in bulk SnO_2, they suffer from high power consumption, low sensitivity, and poor selectivity, and thus further enhancements are highly desired, especially for real-time gas-monitoring applications such as the identification of trace gas biomarkers in human exhaled breath for disease diagnosis and part-per-billion (ppb) hazardous gas monitoring for safety protection.[6, 7]

Hydrogen sulfide (H_2S) is a colorless, flammable, corrosive, and acutely toxic gas that causes deteriorative effect on the olfactory nerves. Trace amounts of H_2S have harmful effects on the eyes, respiratory system, and central nervous system, while inhaling a small amount of highly concentrated H_2S can be fatal in a short period.[8] Besides, H_2S is regarded as an endogenous gas (sub-ppb level) related to disease diagnosis,[9] and thus the sensitive and selective detection of H_2S is highly important. However, most H_2S sensors require high operating temperatures, which are usually above 250 ℃.[10, 11] Although some sensors can operate at lower temperatures, or even at room temperature,[12, 13] they still suffer from poor limit of detection (LOD), which hampers their wide application for sub-ppb H_2S detection.

Gas sensors work based on the direct chemical interaction between sensing materials and analytes. The adsorption of gas molecules (receptor function) and the conversion of chemical signals into electrical signals (transducer function) are the two basic functions of gas sensors. These chemical and electronic interactions between sensing materials and gas molecules are determined by the surface state and electronic characteristics of the sensing materials.[14] Colloidal semiconductor nanocrystals,[15-18] which are also known as quantum dots (QDs) or quantum wires (QWs), have a size of 1~10 nm. Such small sizes of QDs and QWs offer a surface-dominated structure of abundant surface active sites for electronic and chemical interactions in sensing applications.[19] Recently, SnO_2 QDs[20] and QWs[21] that show low-temperature gas-sensing have been reported, but their selectivity and limit of detection (LOD) are still unsatisfactory for practical applications.

Atomic-scale doping provides a powerful way to tailor the electronic properties and surface configuration of semiconductors.[22, 23] Theoretical studies have suggested that the charge transfer between the dopants and host metal oxides would weaken the metal–oxygen bond, promoting the formation of surface oxygen vacancies (V_{O}s).[24] Such point defects created on the surface of semiconductor QDs and QWs can significantly improve the charge carrier density and provide more active sites for the adsorption and surface reactions of gas molecules,[25] improvements that are beneficial to the gas-sensing performance.[26] Traditional doping

---

[a] Department of Applied Biology and Chemical Technology, The Hong Kong Polytechnic University, Hung Hom, Kowloon, Hong Kong SAR, China. E-mail: lawrence.ys.lee@polyu.edu.hk (L. Y. S. Lee)

[b] Department of Applied Physics, The Hong Kong Polytechnic University, Hung Hom, Kowloon, Hong Kong SAR, China.

[c] Research Institute for Smart Energy, The Hong Kong Polytechnic University, Hung Hom, Kowloon, Hong Kong SAR, China.

[d] Institute for Energy Research, Jiangsu University, Zhenjiang, Jiangsu, 212013, China. E-mail: songzl@ujs.edu.cn (Z. Song)

Electronic Supplementary Information (ESI) available: synthesis methods, TEM, XPS, ESR, EPR, SEM, H_2S sensing curve, and LOD analyses of M-SnO_2. Comparison of H_2S gas sensor performances at low temperatures. See DOI: 10.1039/x0xx00000x strategies, such as vacuum or high-temperature ion diffusion and ion implantation, are efficient for bulk semiconductors[27] but they are rarely engaged for semiconductor QDs and QWs due to the self-purification effect that electronically passivates and expels the dopant atoms to the surface.[28, 29] To circumvent this effect, a "remote" doping strategy has been developed, where the ions located in the vicinity of QDs/QWs surface remotely transfer charges to regulate the electronic and chemical properties of QDs/QWs without incorporating the dopant atoms into their lattices.[30, 31] However, such remote doping is only possible with post-synthetic treatment of QDs/QWs solid film, which inevitably alters their interdot spacing and film ordering, causing swelling and/or even destruction of the QD/QW-based sensor films due to the infiltration of the dopant solvent.[32]

Herein, we report the preparation of ultrathin SnO_2 QWs that are doped with transition metal atoms using a general one-step solution process at low temperature (180 °C) and their application in H_2S detection. Systematic characterizations and density functional theory (DFT) calculations indicate that the dopant atoms are adsorbed on the surface of SnO_2 QWs *via* Sn–O–M bond (M = Cr, Mo, and W) and the electron transfer from the dopant atoms to SnO_2 leads to the formation of surface V_O sites. The enriched V_O sites promote the activation of O_2 into the adsorbed active O species and boost the gas-sensing properties. In particular, a gas sensor based on W-doped SnO_2 QWs demonstrates ultrasensitive H_2S detection with a record LOD of 0.48 ppb at a low temperature of 150 ℃ with good long-term stability (~30 days).

Results and discussion

Fig. S1† illustrates the one-step solvothermal process for the preparation of transition-metal-doped SnO_2 (M-SnO_2, M = Cr, Mo, and W) quantum wires (QWs) with the help of oleic acid (OA). For fair comparison, the doping amount of all transition metal atoms was set to 2 at.% relative to the amount of Sn. During the synthesis, OA is deprotonated to OA^- and binds with Sn^{4+} ions to form $Sn(OA)_x$ as the precursor.[33, 34] The $Sn(OA)_x$ is further hydrolyzed during the solvothermal treatment and forms OA^--capped SnO_2 QWs. The surface-bound OA^- can prevent the agglomeration of SnO_2 QWs and make them solution processable.[34] The metal ions would act as short-chain surfactant that competes with the OA/OLA and affects the growth process of SnO_2 QWs.

The transmission electron microscopic (TEM) images of pristine and M-doped SnO_2 QWs (Fig. 1a–d) show that all of them have similar diameters of *ca*. 2~3 nm but with substantial variation in their lengths. The pristine SnO_2 QWs have an average length of 15.9 nm, which is shortened to 12.4, 11.3, and 8.7 nm in Cr-SnO_2, Mo-SnO_2, and W-SnO_2, respectively (Fig. S2a–d†). Apparently, the transition metal doping affects the formation of SnO_2 QWs and shortens the length of the resultant QWs.[35] Density functional theory (DFT) calculations were carried out to figure out the formation mechanism of the M-doped SnO_2 QWs and the results are presented in Fig. 1e–h. The adsorption energies (E_{ads}) of dopant metals (M = Cr, Mo, and W) on the (110) plane of SnO_2 are calculated as −1.74, −2.66, and −3.45 eV, respectively, which are all stronger than that of OA (−0.83 eV) and OLA (−0.44 eV, Fig. S3†). For the pristine SnO_2 QWs, OA plays a critical role in stabilizing the QWs and their growth along the (110) plane due to its relatively strong E_{ads} as well as the larger amount than OLA (10/1, v/v) in the synthesis system. The dopant atoms of more favorable E_{ads} would competitively adsorb on the surface of SnO_2 QWs, slowing down the growth of (110) facets and thus leading to shortened wire lengths. Despite relatively low synthetic temperature (180 ℃), both the pristine and M-doped SnO_2 QWs exhibit a high degree of crystallinity as evidenced by the clear lattice spacings of 0.34 nm (Fig. 1i–l), which correspond to the (110) planes of the tetragonal-rutile-structured SnO_2.[36] The well-retained lattice fringes of the main (110) planes in all samples suggest that the structure of SnO_2 QWs is not altered by metal doping. The energy dispersive spectroscopic (EDS) elemental mapping images shown in Fig. 1m–p confirm the uniform distribution of dopants in the doped samples, and the doping amounts in Cr-SnO_2, Mo-SnO_2, and W-SnO_2 are determined as 1.7, 1.8, and 2.0 at.%, respectively (Table S1†), which are close to the initial feeding ratio of 2 at.%.

The X-ray diffraction (XRD) patterns of the as-prepared samples (Fig. 2a) indicate that all of them have the tetragonal rutile structure of SnO_2 (JCPDS#41-1445) without any other impurities or crystal phases. This confirms the unchanged crystal structure of SnO_2 by metal doping, which is consistent with the TEM results. Fourier-transform infrared (FTIR) spectrum of SnO_2 (Fig. 2b) shows the C−H and $-CH_2$ stretching vibration bands at 2,921, 2,850, 1,459, and 1,397 cm^{-1}, which arise from the long chains of OA and OLA adsorbed on the surface.[37] It is worth noting that the intensities of these bands are largely reduced in the M-SnO_2 QWs. This implies the replacement of OA/OLA by the metal dopants due to their stronger adsorption on the SnO_2 surface, further confirming the role of doped atoms in regulating the microstructure of the SnO_2 QWs. In addition, metal doping also affects the surface state of the SnO_2 QWs, such as metal–oxygen bond. The intensities of the peaks at 683 and 475 cm^{-1}, which are assigned to the Sn−O and O−Sn−O stretching vibrations,[38] respectively, are slightly decreased in M-SnO_2 QWs. This is attributed to the passivation effect of the doped atoms on the surficial oxygen dangling bonds by forming Sn−O−M bonds as predicted by the DFT calculations. In contrast, the peak for the O−H bond[39] is shifted from 1,599 cm^{-1} in SnO_2 to 1,636 cm^{-1} in the M-SnO_2 samples with their peak intensities enhanced. This can be explained by the removal of surface-capped long chains of OA/OLA, which would expose more active sites and facilitate the adsorption of water and oxygen molecules for enhanced gas-sensing performance enhancement.

The doping effect on the surface state was also probed by Raman spectroscopy. As shown in Fig. 2c, the M-SnO_2 samples exhibit obvious changes in their peak intensities. The undoped SnO_2 displays typical A_{1g} and A_s vibration modes at 630 and 575 cm^{-1}, which are attributed to the expansion and contraction of Sn−O bonds and the in-plane V_O positions, respectively.[40] For the cases of the M-SnO_2 samples, the intensity of the A_{1g} peak is much suppressed compared with that of A_s, suggesting that the M doping passivates the Sn−O bonds and forms adjacent V_O sites. The E_g mode band at 426 cm^{-1} in the spectrum of SnO_2 corresponds to the vibration of oxygen atoms in oxygen plane. This band shifts slightly to lower frequencies in Cr-SnO_2 (424 cm^{-1}), Mo-SnO_2 (421 cm^{-1}), and W-SnO_2 (417 cm^{-1}). Also, substantial changes are observed in the intensity ratio of E_u bands (357 and 318 cm^{-1}, local structural symmetry). With W- and Mo-doping, the peak at 318 cm^{-1} is largely suppressed compared with that at 357 cm^{-1}.[41] Both E_g and E_u modes are related to local symmetry changes around the doped metal cations, which result in a disorder/defect of the local structure with the increased scattering intensity of photons from the surface.[42] These results indicate that the dopant atoms perturb and modify the chemical properties and surface state of SnO_2 QWs.

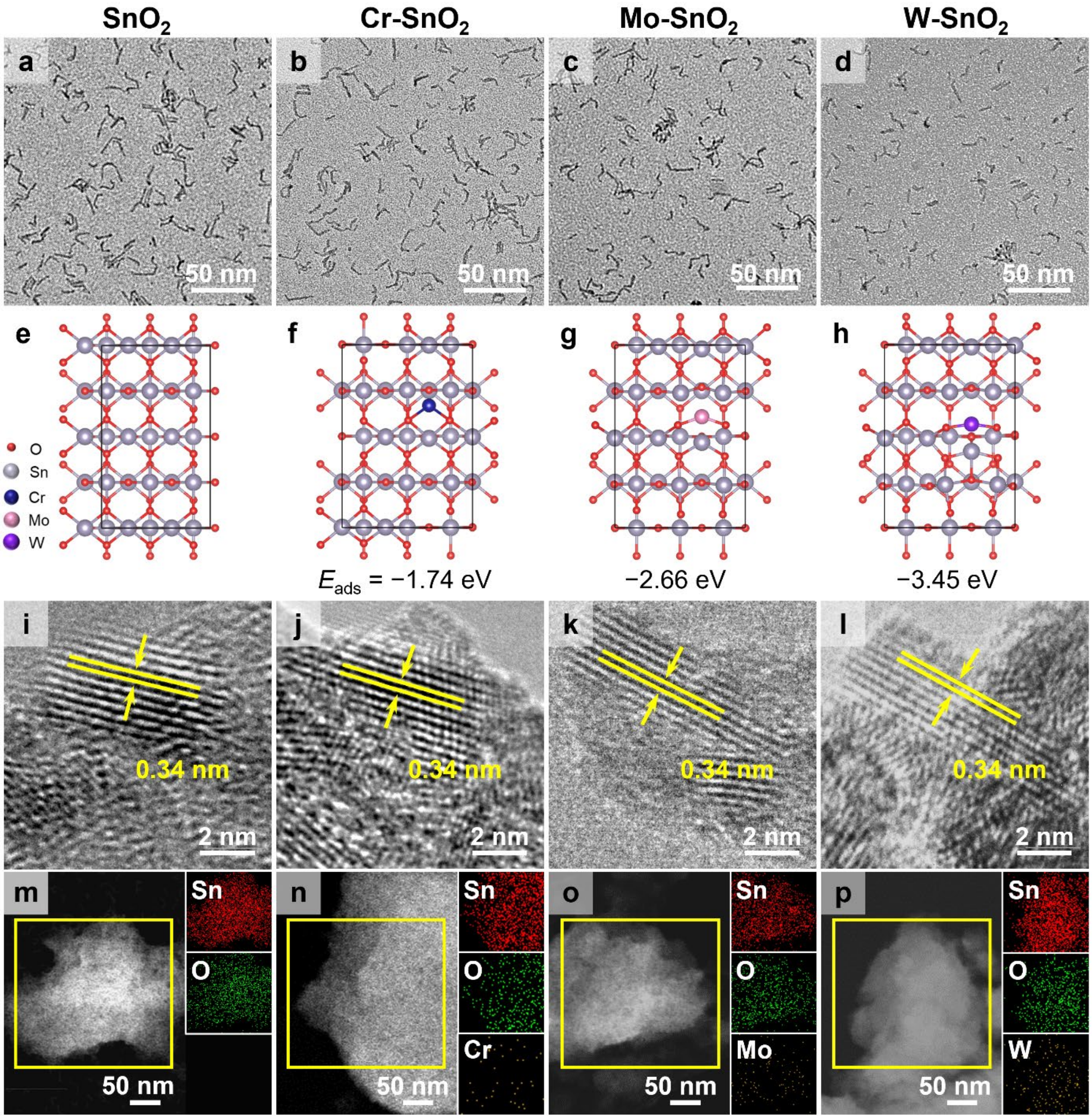

Fig. 1 (a–d) TEM images, (e–h) adsorption energy of doped atom, (i–l) HRTEM images, and (m–p) elemental mapping images of SnO_2, Cr-SnO_2, Mo-SnO_2, and W-SnO_2.

X-ray photoelectron spectroscopy (XPS) was engaged to investigate the surface chemical state and electronic structure of the as-prepared M-SnO_2 QWs. The survey spectra confirm the coexistence of Sn and O elements in all samples (Fig. S4a†). Due to low doping levels, no peaks for the dopant atoms are evident in the survey spectra. However, the high-resolution XPS spectra in Fig. 2d identify the dopant atoms that maintain their initial valence states (Cr^{3+}, Mo^{5+}, and W^{6+} in their respective chloride salts). The high-resolution Sn 3d XPS spectra of the undoped and M-doped SnO_2 QWs (Fig. 2e) exhibit spin–orbital doublets ($3d_{5/2}$ and $3d_{3/2}$) that can be deconvoluted to the two pairs of peaks for dominant Sn^{4+} (*ca*. 495 and 487 eV) and minor Sn^{2+} (*ca*. 494 and 485 eV) species. The existence of Sn^{2+} species in the M-doped SnO_2 QWs was confirmed by a control experiment where the samples were fully oxidized by heating at 550 °C in the air (Fig. S4c). The Sn^{4+} peaks are shifted to higher binding energies in the M-doped SnO_2 QWs in the order of Cr-

SnO_2 (486.9 and 495.3 eV), Mo-SnO_2 (487.0 and 495.4 eV), and W-SnO_2 (487.1 and 495.5 eV) compared with SnO_2 (486.9 and 495.3 eV), indicating electron transfer from Sn to the doped atoms. Similar peak shifts are observed for Sn^{2+} species (Fig. S4b†), and W-SnO_2 shows the highest Sn^{2+} content of 6.2% compared with Mo-SnO_2 (6.1%), Cr-SnO_2 (6.0%), and the undoped SnO_2 (5.0%). This implies that the Sn−O bonds are coordinatively unsaturated with unpaired electrons due to the presence of abundant V_O sites.[43] High-resolution O 1s XPS spectrum of SnO_2 can be split into three peaks of lattice oxygen (O1: 530.8 eV), V_O sites (O2: 531.2 eV), and surface adsorption species (O3: 532.1 eV) (Fig. 2f). The percentage of V_O in W-SnO_2 is calculated to be 38.0%, which is the highest among all the samples (Mo-SnO_2: 34.0%, Cr-SnO_2: 23.2%, and undoped SnO_2: 13.9%). The results of electron spin resonance (ESR) and electron paramagnetic resonance (EPR) measurements are presented in Fig. S5†, and the enhanced signals of the M-doped SnO_2 QWs support the increased V_O sites induced by M-doping.[44, 45] In addition, DFT calculations results (Fig. 2g–j) indicate that W-SnO_2 has the lowest V_O formation energy (5.48 eV) compared with Mo-SnO_2 (5.84 eV), Cr-SnO_2 (5.88 eV), and pristine SnO_2 (6.01 eV) QWs. The abundant V_O sites are expected to adsorb more oxygen species, which would take a critical role in the gas-sensing performance.[46]

We then compared the sensor performance of M-SnO_2 QWs in H_2S sensing. The scanning electron microscopic (SEM) images in Fig. S6† display the as-prepared film samples (thickness = 1 μm) deposited on a micro-heater substrate using a layer-by-layer spin-coating method.[47] Fig. 3a compares the H_2S sensing performances of the samples with the modulation of operation temperature. All three M-SnO_2 samples show enhanced sensing responses ($S = R_a/R_g - 1$, where R_a and R_g are the resistances measured in clean air and in the presence of the target gas, respectively) towards H_2S compared with the undoped one, and the optimal sensing is achieved at 150 °C. Among them, the W-SnO_2 sensor demonstrates the best H_2S-sensing performance (S = 1.33@1,000 ppb), compared with Mo-SnO_2 (S = 1.13@1,000 ppb), Cr-SnO_2 (S = 0.49@1,000 ppb) and pristine SnO_2 sensor (S = 0.15@1000 ppb), and the sensor response is positively correlated with O2 content as shown in Fig. 2f. Fig. 3b and 3c display typical real-time reversible-sensing curves of the M-SnO_2 QW-based gas sensors towards H_2S (0.8 ~ 1,000 ppb), and the sensing curve of

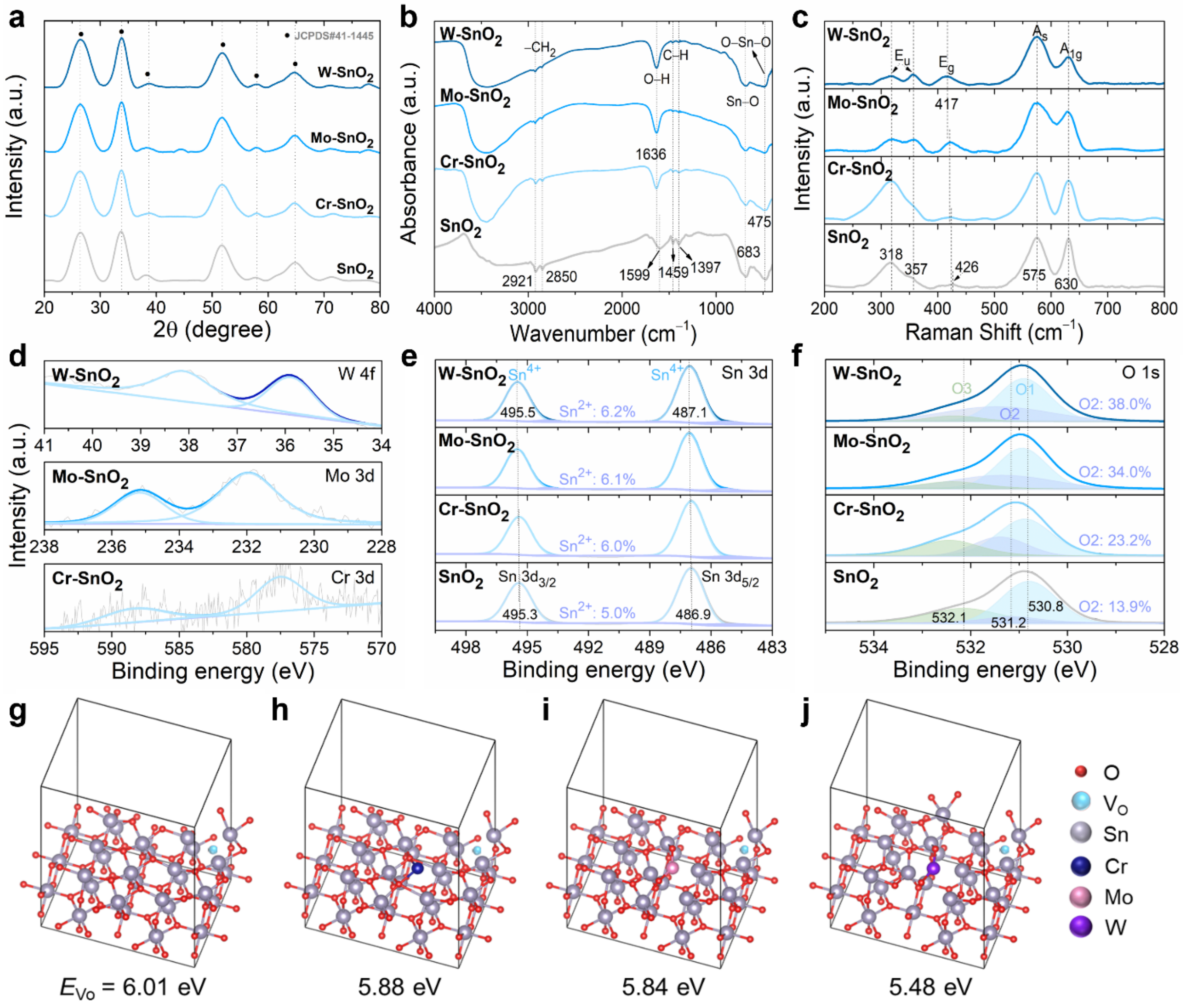

Fig. 2 (a) XRD patterns, (b) FTIR spectra, (c) Raman spectra, and high-resolution XPS spectra of (d) doped elements (W 4f, Mo 3d, and Cr 3d), (e) Sn 3d, and (f) O 1s regions of SnO_2, Cr-SnO_2, Mo-SnO_2, and W-SnO_2. (g–j) Side view of model cell structures on SnO_2 (110) facets of SnO_2, Cr-SnO_2, Mo-SnO_2, and W-SnO_2, respectively.

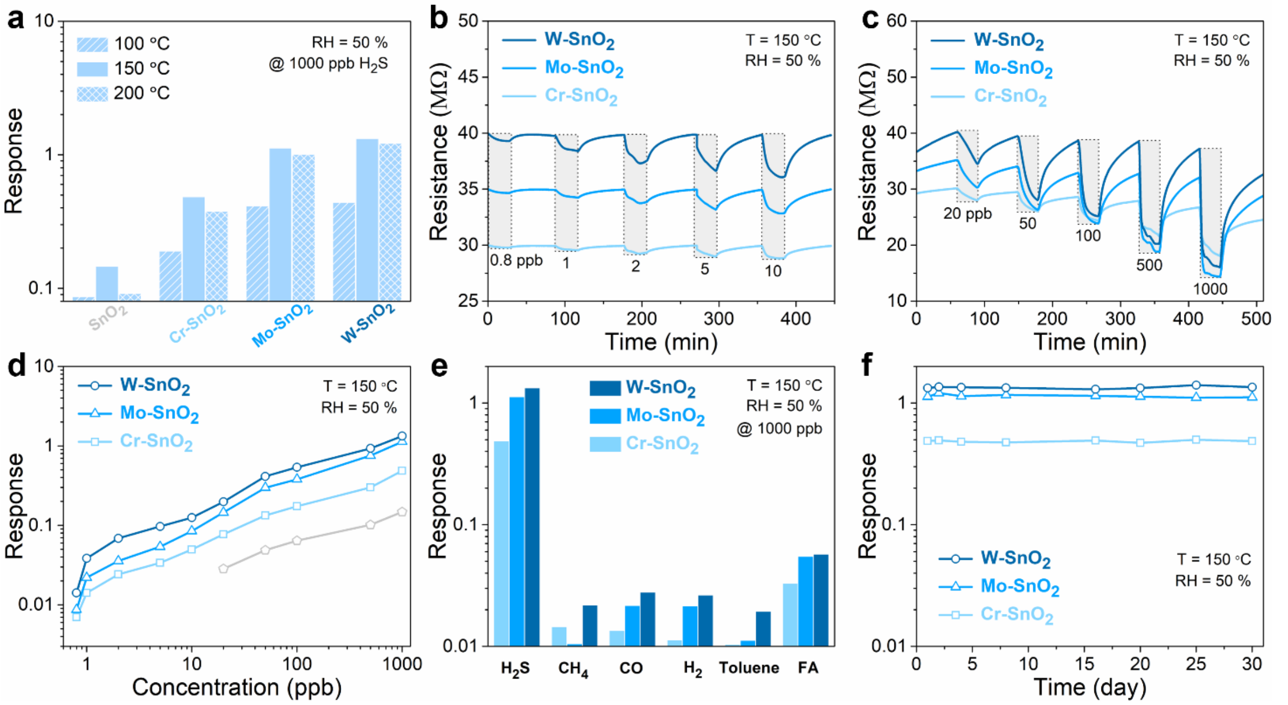

Fig. 3 (a) Sensor responses towards 1,000 ppb H_2S at three operation temperatures of 100, 150, and 200 °C. Typical (b, c) sensing curves and (d) sensor response of W-SnO_2, Mo-SnO_2, and Cr-SnO_2 towards H_2S detection (0.8 ~ 1,000 ppb) at 150 ℃. e) Selectivity of W-SnO_2, Mo-SnO_2, and Cr-SnO_2 sensors for H_2S (1,000 ppb) detection against CH_4, CO, H_2, toluene, and formaldehyde (FA) at 1,000 ppb. f) Long-term stability of the sensors for 1,000 ppb H_2S sensing at 150 ℃.

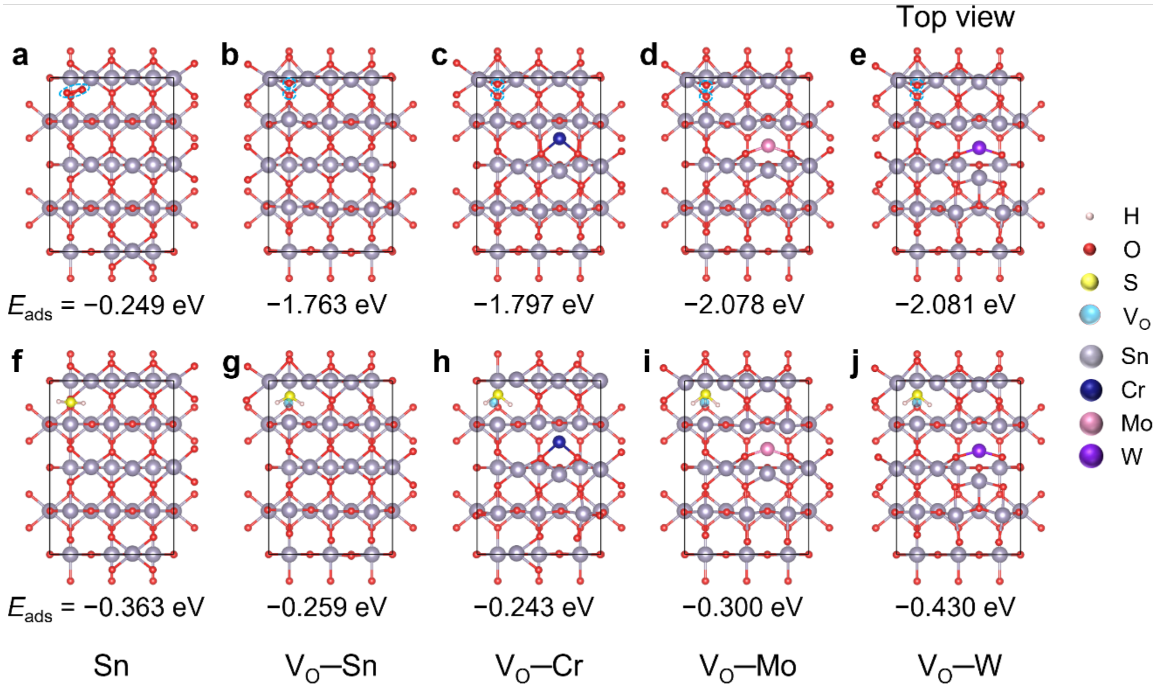

Fig. 4 Top views of the (110) facets of (a, f) pristine SnO_2, (b, g) SnO_2 with V_O sites (c, h) Cr-SnO_2, (d, i) Mo-SnO_2, and (e, j) W-SnO_2, and their calculated O_2 (top panel) and H_2S (bottom panel) adsorption energies (E_{ads}).

the pristine SnO_2 QW sensor is shown in Fig. S7†. The sensing responses were extracted from the sensing curves and summarized in Fig. 3d. All M-SnO_2 QW sensors show enhanced sensing responses compared with the pristine one. The sensing response increases with increasing H_2S concentrations with a minor drift of the baseline resistance (R_a). To clarify the effect of W doping contents, three W-SnO_2 QWs were synthesized using different W/Sn molar ratios (0.5, 2, and 4 %), and their gas-sensing properties are shown in Fig. S8†.

The W-SnO_2-based gas sensor prepared with the W/Sn molar ratio of 2 % shows the best sensing-response towards H_2S. The champion W-SnO_2 QW sensor responses show a linear relationship in the H_2S concentration range between 2 and 50 ppb (Fig. S9†). The slope of the linear fit is 0.00712 ppb^{-1}, and the limit of detection (LOD) is estimated to be 0.48 ppb, according to the following equation:

$$\text{LOD (ppb)} = 3 \times \sigma/\text{slope} \qquad (1)$$

where σ is the standard deviation of noise and calculated as 0.00114 based on 1,000 data points in the baseline of the W-SnO_2 sensor response curve. The W-SnO_2 QW sensor achieves a LOD that is superior to most of the reported metal oxide-based gas sensors (Table S2†), which confirms a positive influence of metal doping on the gas-sensing properties of SnO_2 QWs. In addition, the effect of humidity on the performance of the W-SnO_2-based gas sensor was investigated. The R_a (Fig. S10a†) and their corresponding sensing response (Fig. S10b†) decrease with the increasing RH from 0 to 70 %. It is believed that the water vapor consumes the active sites for sensing and forms less reactive hydroxyl groups (OH), causing changes in the sensor resistance and deteriorating sensing response.[48, 49] Our sensors also show excellent selectivity toward H_2S from the tests with the interfering gases of CH_4, CO, H_2, toluene, and formaldehyde (Fig. 3e). Given that the gas-sensing reaction requires the activation energy for gas adsorption and chemical bonds breaking, H_2S has the smallest bond energy of H–SH compared with the interfering gas molecules (CH_4, CO, and H_2, Table S3†). Although toluene and formaldehyde have smaller bond energies, the favorable chemical interaction of H_2S with the surface adsorbed oxygen species due to strong reducing capability[50, 51] contributes to the H_2S selectivity of our sensor. Furthermore, all M-SnO_2 sensors show good long-term stability as evidenced by H_2S detection with a minor fluctuation after 30 days (Fig. 3f).

DFT calculations were performed to evaluate E_{ads} of gas molecules on the sensing materials (Fig. 4). All the configurations of gas molecules (O_2, H_2S) on the surface of the undoped SnO_2 without V_O (Fig. 4a and 4f) and with V_O (Fig. 4b and 4g), and Cr- (Fig. 4c and 4h), Mo- (Fig. 4d and 4i), and W-doped (Fig. 4e and 4j) SnO_2 were considered. The E_{ads} of O_2 on the undoped SnO_2 with and without V_O are calculated to be −1.763 and −0.249 eV, respectively. It was reported that the V_O on the SnO_2 can dissociate the O_2 molecules into active oxygen (O^-) species, strengthening the O_2 adsorption capability and surface reactions.[52, 53] The E_{ads} of O_2 on the doped SnO_2 are calculated to be all stronger than that of undoped SnO_2 regardless of the presence of V_O (Cr-SnO_2: −1.797; Mo-SnO_2: −2.078; and W-SnO_2: −2.081 eV), and thus more O_2 are adsorbed on the M-SnO_2 samples to form more active oxygen (O^-) species. This is consistent with the O 1s XPS results. The E_{ads} of the target H_2S molecules on the undoped SnO_2 with and without V_O are calculated to be −0.259 and −0.363 eV, respectively, a result that shows a negligible effect of V_O on H_2S adsorption. The E_{ads} of H_2S on the Cr-, Mo-, and W-doped SnO_2 are −0.243, −0.300, and −0.430 eV, respectively, and the slight increment of the E_{ads} of H_2S can be attributed to the doped atoms regardless of the formed V_O. According to the sensing response and the calculated E_{ads} of O_2 and H_2S, the stronger E_{ads} of O_2 can be correlated to the higher sensing response. Based on our characterization results and DFT calculations, a sensing mechanism is proposed to illustrate the effect of doping on the sensing performance of SnO_2 QW-sensor: the increased V_O density due to metal doping induces more oxygen chemisorption, and this produces an electron depletion layer on the SnO_2 surface ($O_2 + e^- \rightarrow O^-$) and increases the R_a as evidenced by 29.7, 35.4, and 40.4 MΩ for Cr-, Mo-, and W-SnO_2 QWs, respectively (Fig. 3b). Ultimately, the target H_2S gas reacts with the adsorbed oxygen species ($H_2S + O^- \rightarrow SO_2 + H_2O + e^-$), releasing the trapped electron back to SnO_2 and resulting in a decreased resistance, thus leading to an enhanced gas-sensing response.[54, 55]

Conclusions

We demonstrated a general route to realize the transition metal-doped ultrathin SnO_2 QWs. The transition metal atom (Cr, Mo, and W) doping in SnO_2 QWs enabled the tailoring of electronic structures by reducing the energy barrier for O_2 molecule adsorption and activation and accelerating surface reaction kinetics with H_2S molecules. As a result, the optimized metal-doped SnO_2 QW-based gas sensors possess excellent sub-ppb level H_2S-sensing capability with excellent selectivity at the relatively low operating temperature of 150 °C. This work provides detailed studies on the electronic engineering of metal doping of colloidal nanocrystals by modulating oxygen vacancies for ultrahigh gas-sensing performance.

Experimental

Chemicals

All chemicals were used as received without further purification. Stannic chloride hydrated ($SnCl_4 \cdot 5H_2O$, 99.95%), chromium chloride hexahydrate ($CrCl_3 \cdot 6H_2O$, 98%), molybdenum pentachloride ($MoCl_5$, 99.6%), tungsten chloride (WCl_6, 99.9%), vanadium(III) chloride (VCl_3, 99%), niobium chloride ($NbCl_5$, 99.9%), tantalum chloride anhydrous ($TaCl_5$, 95%), oleic acid (OA, 99%), oleylamine (OLA, 80–90%), 5,5-dimethyl-1-pyrroline *N*-oxide ethanol (DMPO, >98%), and *n*-hexane (95%) were purchased from Sigma–Aldrich.

Synthesis of M-SnO_2

M-SnO_2 QWs were synthesized using a direct solvothermal method. To an ethanolic solution (10 mL) containing $SnCl_4 \cdot 5H_2O$ (1 mmol) and a chloride salt of transition metal ($CrCl_3$, $MoCl_5$, WCl_6, VCl_3, $NbCl_5$, and $TaCl_5$, 0.02 mmol), oleic acid (OA, 20 mL) and oleylamine (OLA, 2 mL) were added and stirred at room temperature until a clear solution was obtained. The solution was transferred into a 50 mL Teflon-lined stainless-steel autoclave and the temperature was increased to 180 °C and kept for 6 h. The product was collected by filtration, rinsed with *n*-hexane and ethanol several times to remove the residual OA and OLA, and dispersed in ethanol at a concentration of 10 mg mL^{-1}. SnO_2 QWs were obtained by the same procedure in the absence of chloride salt.

Characterizations of materials

Transmission electron microscopy (TEM) and scanning TEM (STEM) were performed using a JEOL JEM-2100F TEM/STEM operated at 200 kV. Samples for TEM analysis was prepared by drop-casting the samples dispersed in water onto a holey carbon-coated 400 mesh Cu TEM grid. The elemental composition of samples was determined by an energy dispersive spectrometer (EDS) equipped in the TEM. Scanning electron microscopic (SEM) images were obtained using a TESCAN VAGA3 (TESCAN, USA). X-ray diffractometer (XRD, Rigaku SmartLab 9KW-Advance) with Cu Kα radiation (λ = 1.5406 Å) was used for investigating the crystal structure of samples from 20 to 80° (2θ) with a step size of 0.02° at a rate of 10° min^{-1}. Fourier-transform infrared spectra (FTIR) were obtained between 4,000 and 400 cm^{-1} on an FTIR spectrometer (Nexus 470, Thermo Electron Corporation). Raman spectra were recorded from 200 to 800 cm^{-1} on a Raman spectrometer (Confocal Micro-Raman Spectroscopy System, Renishaw) using a 532 nm laser. The surface chemical compositions and oxidation states of samples were characterized by X-ray photoelectron spectroscopy (XPS) using an AXIS-His spectrometer with Al Kα radiation and pass energy of 1,486.6 eV. Electron spin resonance (ESR) analysis was conducted on a Bruker model ESR JES-FA200 spectrometer using the spin-trapping reagent DMPO. Electron paramagnetic resonance (EPR) spectra were collected using an ADANI SPINSCAN X spectrometer with an operating microwave frequency of 9.390 GHz at room temperature.

Fabrication of sensor device

A layer-by-layer spin-coating deposition technique was used for the fabrication of the sensor device. On an Al_2O_3 substrate patterned with interdigital Ag–Pd electrodes, the as-obtained sample solution (50 μL) was drop-cast and spun at 1,500 rpm for 30 s, and this step was repeated three times. Finally, the deposited sample film was washed with ethanol and spun dry three times.

Gas-sensing measurements

The sensor device was placed in a test chamber and a target gas was purged at a total gas flow rate of 500 $cm^3\ min^{-1}$ controlled by a mass flow controller (MFC). The sensor resistance was continuously recorded upon gas exposure or release using a Keithley 2450 source meter (Keithley Instrument, U.S.A.). The sensor response ($S = R_a/R_g$) was defined as the ratio of resistance in the presence of clean air (R_a) to the resistance in the presence of the target gas (R_g).

Density functional theory (DFT) calculations

All DFT calculations were conducted based on the Vienna *ab initio* simulation package (VASP).[56] The electron–ion interactions were described by the projected augmented-wave (PAW) potentials, while the exchange-correlation interactions were calculated by employing the Perdew–Burke–Ernzerhof (PBE) functional with Hubbard U corrections (PBE + U) of generalized gradient approximation (GGA),[57, 58] which we employed as (U − J) = 3.70, 4.38, and 6.20 eV for Cr, Mo, and W, respectively. The vdW-D3 method was employed to describe the van der Waals interaction,[59] taking the spin-polarized set into account with the plane-wave energy cutoff set at 450 eV. The convergence threshold was set as 1.0×10^{-6} eV in energy and 0.02 eV $Å^{-1}$ in force. The slab model was constructed on the (110) facet of the optimized bulk SnO_2. A vacuum layer of 15 Å was adopted to avoid periodic interactions. The Brillouin zone was modeled by gamma centered Monkhorst-Pack scheme, in which a 3 × 2 × 1 grid was adopted for all slab models.

Author Contributions

J. Y. and Z. S. designed this study, contributed to all the experimental work, analyzed the data, wrote the manuscript, and funding support. Y. Z. and X. G. helped with the manuscript discussion. L. Y. S. L. contributed to conceptualization, funding acquisition, supervision, writing review & editing.

Conflicts of interest

There are no conflicts to declare.

Acknowledgements

We gratefully acknowledge the financial support from The Hong Kong Polytechnic University (Q-CDA3), the Research Grants Council of the Hong Kong Special Administrative Region (Project No. PolyU15217521), and the National Natural Science Foundation of China (62004084 and 22106053).

References

1. Z. Song, W. Ye, Z. Chen, Z. Chen, M. Li, W. Tang, C. Wang, Z. Wan, S. Poddar, X. Wen, X. Pan, Y. Lin, Q. Zhou and Z. Fan, *ACS Nano*, 2021, **15**, 7659-7667.
2. S. Guo, D. Yang, S. Zhang, Q. Dong, B. Li, N. Tran, Z. Li, Y. Xiong and M. E. Zaghloul, *Adv. Funct. Mater.*, 2019, **29**, 1900138.
3. I. C. Weber, H. P. Braun, F. Krumeich, A. T. Guntner and S. E. Pratsinis, *Adv. Sci.*, 2020, **7**, 2001503.
4. Q. Hu, C. Wu, Z. Dong, G. Zhang, Z. Ma, X. Wang, S. Sun and J. Xu, *J. Mater. Chem. A*, 2022, **10**, 2786-2794.
5. P. Wu, Y. Li, S. Xiao, J. Chen, J. Tang, D. Chen and X. Zhang, *J. Hazard. Mater.*, 2022, **422**, 126882.
6. K. Suematsu, T. Oyama, W. Mizukami, Y. Hiroyama, K. Watanabe and K. Shimanoe, *ACS Appl. Electron. Mater.*, 2020, **2**, 2913-2920.
7. P. G. Choi, N. Izu, N. Shirahata and Y. Masuda, *Sens. Actuators B Chem.*, 2019, **296**, 126655.
8. N. N. Greenwood and A. Earnshaw, *Chemistry of the Elements*, Elsevier-Butterworth Heinemann, Amsterdam, The Netherlands, 2016.
9. D. J. Polhemus and D. J. Lefer, *Circ Res.*, 2014, **114**, 730-737.
10. J. Bao, Z. Zhang and Y. Zheng, *Sens. Actuators B Chem.*, 2021, **345**, 130408.
11. R. K. Jain and A. Khanna, *Sens. Actuators B Chem.*, 2021, **343**, 130153.
12. H. He, C. Zhao, J. Xu, K. Qu, Z. Jiang, Z. Gao and Y. Y. Song, *ACS Sens.*, 2021, **6**, 3387-3397.
13. C. Zhang, K. Wu, H. Liao and M. Debliquy, *Chem. Eng. J.*, 2022, **430**, 132813.
14. X. Chen, T. Wang, J. Shi, W. Lv, Y. Han, M. Zeng, J. Yang, N. Hu, Y. Su, H. Wei, Z. Zhou, Z. Yang and Y. Zhang, *Nano-Micro Lett.*, 2021, **14**, 8.
15. P. G.-S. Moonsub Shim, *Nature*, 2000, **407**, 981-983.
16. M. Li, C. Wang, L. Wang and H. Zhang, *J. Mater. Chem. C*, 2021, **9**, 6686-6721.
17. J. Zito and I. Infante, *Acc. Chem. Res.*, 2021, **54**, 1555-1564.

18. V. Lesnyak, *J. Phys. Chem. Lett.*, 2021, **12**, 12310-12322.
19. T. Russ, Z. Hu, B. Junker, H. Liu, U. Weimar and N. Barsan, *J. Phys. Chem. C*, 2021, **125**, 19847-19857.
20. H. Liu, S. Xu, M. Li, G. Shao, H. Song, W. Zhang, W. Wei, M. He, L. Gao, H. Song and J. Tang, *Appl. Phys. Lett.*, 2014, **105**, 163104.
21. Z. Song, S. Xu, M. Li, W. Zhang, H. Yu, Y. Wang and H. Liu, *Thin Solid Films*, 2016, **618**, 232-237.
22. Y. Feng, J. Wu, Q. Chi, W. Li, Y. Yu and W. Fei, *Chem. Rev.*, 2020, **120**, 1710-1787.
23. A. Ghosh, O. F. Mohammed and O. M. Bakr, *Acc. Chem. Res.*, 2018, **51**, 3094-3103.
24. A. Ruiz Puigdollers, P. Schlexer, S. Tosoni and G. Pacchioni, *ACS Catal.*, 2017, **7**, 6493-6513.
25. H. Yuan, S. Aljneibi, J. Yuan, Y. Wang, H. Liu, J. Fang, C. Tang, X. Yan, H. Cai, Y. Gu, S. J. Pennycook, J. Tao and D. Zhao, *Adv. Mater.*, 2019, **31**, 1807161.
26. D. Yao, C. Dong, Q. Bing, Y. Liu, F. Qu, M. Yang, B. Liu, B. Yang and H. Zhang, *ACS Appl. Mater. Interfaces*, 2019, **11**, 23495-23502.
27. S.-Y. Kuo, W.-C. Chen, F.-I. Lai, C.-P. Cheng, H.-C. Kuo, S.-C. Wang and W.-F. Hsieh, *J. Cryst. Growth*, 2006, **287**, 78-84.
28. G. M. Dalpian and J. R. Chelikowsky, *Phys. Rev. Lett.*, 2006, **96**, 226802.
29. C. R. Kagan, E. Lifshitz, E. H. Sargent and D. V. Talapin, *Science*, 2016, **353**, 885.
30. J. H. Engel, Y. Surendranath and A. P. Alivisatos, *J. Am. Chem. Soc.*, 2012, **134**, 13200-13203.
31. A. R. Kirmani, G. H. Carey, M. Abdelsamie, B. Yan, D. Cha, L. R. Rollny, X. Cui, E. H. Sargent and A. Amassian, *Adv. Mater.*, 2014, **26**, 4717-4723.
32. M. C. Weidman, K. G. Yager and W. A. Tisdale, *Chem. Mater.*, 2014, **27**, 474-482.
33. W. Bu, Z. Chen, F. Chen and J. Shi, *J. Phys. Chem. C*, 2009, **113**, 12176-12185.
34. X. Xu, J. Zhuang and X. Wang, *J. Am. Chem. Soc.*, 2008, **130**, 12527-12535.
35. Z. Song, Z. Hu, J. Liu, J. Yan, H. Li, J. Jiang, J. Tang and H. Liu, *Adv. Electron. Mater.*, 2021, **7**, 2101049.
36. V. Bonu, A. Das, S. Amirthapandian, S. Dhara and A. K. Tyagi, *Phys. Chem. Chem. Phys.*, 2015, **17**, 9794-9801.
37. S. Mourdikoudis and L. M. Liz-Marzán, *Chem. Mater.*, 2013, **25**, 1465-1476.
38. B. Zhang, Y. Tian, J. X. Zhang and W. Cai, *Mater. Lett.*, 2011, **65**, 1204-1206.
39. N. C. Horti, M. D. Kamatagi, N. R. Patil, M. N. Wari and S. R. Inamdar, *Optik*, 2018, **169**, 314-320.
40. L. Z. Liu, X. L. Wu, F. Gao, J. C. Shen, T. H. Li and P. K. Chu, *Solid State Commun.*, 2011, **151**, 811-814.
41. A. Diéguez, A. Romano-Rodríguez, A. Vilà and J. R. Morante, *J. Appl. Phys.*, 2001, **90**, 1550-1557.
42. I. M. Costa, Y. N. Colmenares, P. S. Pizani, E. R. Leite and A. J. Chiquito, *Chem. Phys. Lett.*, 2018, **695**, 125-130.
43. L. Villamagua, A. Stashans, M. Carini and F. Maldonado, *AIP Adv.*, 2016, **6**, 115217.
44. M. Shao, J. Liu, W. Ding, J. Wang, F. Dong and J. Zhang, *J. Mater. Chem. C*, 2020, **8**, 487-494.
45. J. Wu, Q. Huang, D. Zeng, S. Zhang, L. Yang, D. Xia, Z. Xiong and C. Xie, *Sens. Actuators B Chem.*, 2014, **198**, 62-69.
46. Y. Xiao, Y. Wang, M. Xiao, C. Liu, S. Hou, J. Ge and W. Xing, *NPG Asia Mater.*, 2020, **12**, 73.
47. R. S. Niranjan and I. S. Mulla, *Mater. Sci. Eng. B*, 2003, **103**, 103-107.
48. S. Y. Jeong, Y. K. Moon, J. K. Kim, S. W. Park, Y. K. Jo, Y. C. Kang and J. H. Lee, *Adv. Funct. Mater.*, 2020, **31**, 2007895.
49. J. W. Yoon, J. S. Kim, T. H. Kim, Y. J. Hong, Y. C. Kang and J. H. Lee, *Small*, 2016, **12**, 4229-4240.
50. S. Yang, J. Sun, L. Xu, Q. Zhou, X. Chen, S. Zhu, B. Dong, G. Lu and H. Song, *Sens. Actuators B Chem.*, 2020, **324**, 128725.
51 J. Wu, Y. Yang, C. Zhang, H. Yu, L. Huang, X. Dong, J. Wang and X. Wang, *Dalton Trans.*, 2019, **48**, 7720-7727.
52. A. Gurlo, *Chemphyschem*, 2006, **7**, 2041-2052.
53. B. Slater, C. R. A. Catlow, D. E. Williams and A. M. Stoneham, *Chem. Commun.*, 2000, **36**, 1235-1236.
54. H. Liu, S. P. Gong, Y. X. Hu, J. Q. Liu and D. X. Zhou, *Sens. Actuators B Chem.*, 2009, **140**, 190-195.
55. P. Bellare, N. Sakhuja, S. Kundu, N. Bhat and N. Ravishankar, *ACS Appl. Nano Mater.*, 2020, **3**, 3730-3740.
56. G. Kresse and J. Furthmuller, *Comput. Mater. Sci.*, 1996, **6**, 15-50.
57. P. E. Blochl, *Phys. Rev. B*, 1994, **50**, 17953-17979.
58. J. P. Perdew, K. Burke and M. Ernzerhof, *Phys. Rev. Lett.*, 1997, **78**, 1396-1396.
59. S. Grimme, J. Antony, S. Ehrlich and H. Krieg, *J. Chem. Phys.*, 2010, **132**, 154104.